CrossMark

ORIGINAL ARTICLE

Tim Dally · **Kerstin Weinberg**

The phase-field approach as a tool for experimental validations in fracture mechanics

Abstract In a phase-field approach to fracture crack propagation is modeled by means of an additional continuous field. In this paper, two problems of linear elastic fracture mechanics are studied experimentally and numerically in order to evaluate the practicability of the phase-field approach and to validate the measured parameters. At first, a three-point bending experiment of silicon dies is simulated assuming static plate bending. Then, wave propagation and spallation in a Hopkinson bar test are analyzed in a dynamic regime. The simulations show that phase-field fracture reproduces the experimental results with high accuracy. The results are comparable to other fracture simulations, e.g., the cohesive element technique. In total, the phase-field approach to fracture is capable of tracking crack evolution in a very convenient and quantitatively correct way.

1 Introduction

Phase-field methods gained raising attention for the simulation of fracture and crack propagation, see, e.g., [4,9,14,16,26]. The main idea of a phase-field approach is to replace the sharp boundary of a crack by a "smeared" crack zone. An additional order parameter—the phase field $\mathfrak{s}(x, t)$—marks the virgin state ($\mathfrak{s} = 1$) and the broken state ($\mathfrak{s} = 0$) of the material, where the evolution of the phase field follows an additional partial differential equation. Similar to level set methods, this approach allows for an efficient computation of moving boundaries and arbitrary crack pattern [18,23]. Obviously, the exact form of the evolution equation has to reflect the physics of fracture mechanics and needs to depend on the specific properties of the material.

The ability of the phase-field method to simulate crack propagation and sophisticated fracture pattern in the static and in the dynamic regime has been shown in several recent simulations [3,10,15,17]. In this paper, the accuracy of such an approach is critically evaluated. To this end, we study two problems of linear elastic fracture mechanics in the sense of an inverse analysis and compare our experimental results with phase-field fracture simulations. Intentionally, we restrict our comparison to materials which can be modeled as linear elastic and ideally brittle. The extension of phase-field fracture to the finite deformation range is straightforward, cf. [11], but it faces the problem of predictability in a similar manner.

The paper is organized as follows: In Sect. 2, the basic equations for the finite element simulations in the frame of linear elastic fracture mechanics are summarized, and the influence of the model parameter on the solution is illustrated. In Sect. 3, an analysis of a three-point bending experiment of silicon dies is provided.

T. Dally (✉) · K. Weinberg
Lehrstuhl für Festkörpermechanik, Institut für Mechanik und Regelungstechnik, Fakultät IV, Universität Siegen
Paul-Bonatz-Straße 9-11, 57068 Siegen, Germany
E-mail: tim.dally@uni-siegen.de

This plate bending problem illustrates the possibilities of phase-field fracture simulations to determine the fracture energy in a static problem. Section 4 describes the analysis of a Hopkinson bar spalling experiment. The material studied here is a newly developed ultra-high-performance concrete whose dynamic properties have been investigated in a previous work [13]. A short summary compares the phase-field method of fracture with established methods like the cohesive element technique.

2 Phase-field approach to linear elastic fracture

We consider an arbitrary structure of domain $\Omega \subset \mathbb{R}^d$ and dimension $d = 2, 3$ with external boundary $\partial \Omega$. The structure's displacement field at point $\boldsymbol{x}$ and time t is $\boldsymbol{u}(\boldsymbol{x}, t)$; its velocity and acceleration fields are $\boldsymbol{v} = \dot{\boldsymbol{u}}$ and $\boldsymbol{a} = \ddot{\boldsymbol{u}}$. The displacements satisfy the Dirichlet boundary conditions $\boldsymbol{u} = \bar{\boldsymbol{u}}$ at $\Gamma_0 \subset \Gamma$. The structure is loaded with traction $\bar{\boldsymbol{q}}$ at boundary $\Gamma_1 \subset \Gamma$, additional initial conditions may be given. In general, it holds the balance of linear momentum,

$$\operatorname{div} \boldsymbol{\sigma} + \bar{\boldsymbol{p}} = \rho \ddot{\boldsymbol{u}} , \tag{1}$$

where $\boldsymbol{\sigma}$ is the elastic stress tensor and ρ the mass density of the structure and $\bar{\boldsymbol{p}}$ a prescribed body force. We assume small deformations with strain tensor $\boldsymbol{\epsilon} \in \mathbb{R}^{d \times d}$.

$$\boldsymbol{\epsilon} = \frac{1}{2} \left(\nabla \boldsymbol{u} + \nabla \boldsymbol{u}^T \right) \tag{2}$$

The linear elastic material is presumed to follow Hooke's law with elastic strain energy density, $\Psi^e = \frac{1}{2}\lambda(\operatorname{tr}\boldsymbol{\epsilon})^2 + \mu\boldsymbol{\epsilon} : \boldsymbol{\epsilon}$, or, more generally formulated with Hooke's tensor $\mathbb{C}$,

$$\Psi^e(\boldsymbol{u}) = \frac{1}{2}\boldsymbol{\epsilon}(\boldsymbol{u}) : \mathbb{C} : \boldsymbol{\epsilon}(\boldsymbol{u}). \tag{3}$$

Now, let the boundaries of the evolving internal cracks be represented by a set $\Gamma(t)$. According to linear elastic fracture mechanics of Griffith and Irwin [8,12], a material fails upon attainment of a critical fracture energy density G_c. The crack growth corresponds to the creation of new surfaces, and hence, the total potential energy of the structure is composed of

$$W(\boldsymbol{u}, t) = \int_\Omega \Psi^e(\boldsymbol{u}) \, \mathrm{d}\Omega + \int_{\Gamma(t)} G_c \, \mathrm{d}\Gamma. \tag{4}$$

An optimum of (4) describes crack growth. However, for an unknown crack set $\Gamma(t)$, this variational problem cannot be solved in general.

In order to represent the evolving cracks in the phase-field approach to fracture, an additional continuous field $\mathfrak{s}$ is introduced,

$$\mathfrak{s}(\boldsymbol{x}, t) \in [0, 1] \quad \forall \boldsymbol{x} \in \Omega, \ t \in \mathbb{R} , \tag{5}$$

which has a value of $\mathfrak{s} = 1$ in the intact material and indicates the 'cracked zones' with a value of $\mathfrak{s} = 0$. Continuity of (5) requires a transition zone between both phases. Such a transition zone cannot reflect the sharp boundary of a crack but models a diffuse interface of width $2l_c$ instead. Thus, in a phase-field approach, the crack set $\Gamma(t)$ is replaced by a regularizing crack density functional $\gamma(t)$.

$$\int_{\Gamma(t)} G_c \, \mathrm{d}\Gamma \approx \int_\Omega \gamma(t) \, \mathrm{d}\Omega \tag{6}$$

Now following the ansatz of [1,7], the corresponding total potential energy reads

$$W(\boldsymbol{u}, \mathfrak{s}) = \int_\Omega \Psi^e(\boldsymbol{u}) \, \mathrm{d}\Omega + \int_\Omega \gamma(\mathfrak{s}(t)) \, \mathrm{d}\Omega$$
$$= \int_\Omega \underbrace{\left(\frac{1}{2}\boldsymbol{\epsilon} : \mathbb{C}^* : \boldsymbol{\epsilon} + G_c \left(\frac{1}{4l_c}(1 - \mathfrak{s})^2 + l_c |\nabla\mathfrak{s}|^2 \right) \right)}_{\psi} \, \mathrm{d}\Omega. \tag{7}$$

The tensor $\mathbb{C}^*$ in the elastic part of the strain energy density is constituted by means of a substitute material approach,

$$\mathbb{C}^* = (\mathfrak{s}^2 + \eta)\mathbb{C}, \quad \eta \ll 1,$$

which also accounts for the 'empty' crack. The small parameter η is only introduced to avoid numerical problems in damaged material. At this point, an evolution equation for the phase-field parameter $\mathfrak{s}$ can be stated in the sense of an Allen–Cahn equation,

$$\dot{\mathfrak{s}} = -M\frac{\delta\Psi}{\delta\mathfrak{s}} = -M\left[\boldsymbol{\epsilon} : \mathbb{C} : \boldsymbol{\epsilon}\mathfrak{s} - G_c\left(2l_c\Delta\mathfrak{s} + \frac{1-\mathfrak{s}}{2l_c}\right)\right], \tag{8}$$

where M is a positive mobility constant. However, the quadratic form of the elastic strain energy density does not distinguish between tensile and pressure states in the material. A direct use of the formulations (7) or (8) would allow a crack to grow also in the compressive regime which clearly contradicts the physics of the underlying problem. For that reason, a split of the elastic strains has been performed, $\boldsymbol{\epsilon} = [\boldsymbol{\epsilon}^+] + [\boldsymbol{\epsilon}^-]$, where $[\boldsymbol{\epsilon}^+]$ denotes the positive and tensile components of the principal strains, and $[\boldsymbol{\epsilon}^-]$ the remaining compressive parts. This leads to an elastic energy density function which only accounts for tension.

$$\Psi^{e+} = \frac{1}{2}[\boldsymbol{\epsilon}^+] : \mathbb{C}^* : [\boldsymbol{\epsilon}^+] \tag{9}$$

In that way, a physical consistent fracture criterion has been defined. Note, that this approach differs from the decomposition of strains in volumetric and deviatoric tensional parts as suggested in [16] and for finite deformations also in [11].

2.1 Discretization

By multiplication of the Eqs. (1) and (8) with arbitrary but suitable test functions $\boldsymbol{w}, \mathfrak{v} \in \mathcal{V}$, integration over the domain Ω, and an application of Gauss' theorem, the weak form of the coupled problem is obtained.

$$\int_\Omega \operatorname{grad}\boldsymbol{w} : \operatorname{div}\boldsymbol{\sigma}\,\mathrm{d}\Omega - \int_\Omega \boldsymbol{w} \cdot \bar{\boldsymbol{p}}\,\mathrm{d}\Omega + \int_\Omega \boldsymbol{w} \cdot \rho\ddot{\boldsymbol{u}}\,\mathrm{d}\Omega - \int_{\Gamma_1} \boldsymbol{w} \cdot \bar{\boldsymbol{q}}\,\mathrm{d}\Gamma_1 = 0 \tag{10}$$

$$\frac{1}{M}\int_\Omega \dot{\mathfrak{s}}\mathfrak{v}\,\mathrm{d}\Omega + \int_\Omega (\boldsymbol{\epsilon} : \mathbb{C} : \boldsymbol{\epsilon})\,\mathfrak{s}\mathfrak{v}\,\mathrm{d}\Omega + 2G_c l_c\int_\Omega \nabla\mathfrak{s}\nabla\mathfrak{v}\,\mathrm{d}\Omega - \frac{G_c}{2l_c}\int_\Omega (1-\mathfrak{s})\mathfrak{v}\,\mathrm{d}\Omega = 0 \tag{11}$$

The geometric discretization is performed employing finite elements where the displacements $\boldsymbol{u}$ and the phase-field parameter $\mathfrak{s}$ as well as the corresponding test functions are approximated with piecewise linear shape functions summarized in the vector $\mathbf{N} = [N_i]$:

$$\boldsymbol{u} = \sum_{i=1}^n N_i\boldsymbol{u}_i, \quad \mathfrak{s} = \sum_{i=1}^n N_i s_i,$$
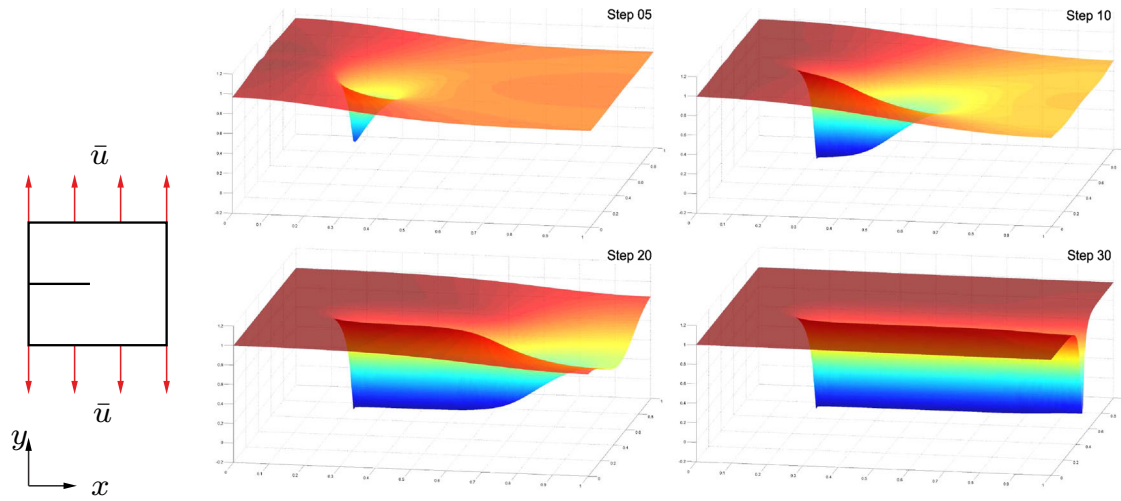
The discretization of Eq. (10) results in the system

$$\tilde{\mathbf{M}}\ddot{\mathbf{u}} + \tilde{\mathbf{K}}\mathbf{u} = \tilde{\mathbf{f}}$$

with

$$\tilde{\mathbf{M}} = \int_\Omega \rho\mathbf{N}\mathbf{N}^T\,\mathrm{d}\Omega, \quad \tilde{\mathbf{K}} = \int_\Omega \nabla\mathbf{N}\mathbb{C}^*\nabla\mathbf{N}^T\,\mathrm{d}\Omega, \quad \tilde{\mathbf{f}} = \int_\Omega \mathbf{N}\bar{\boldsymbol{p}}\,\mathrm{d}\Omega + \int_{\Gamma_1} \mathbf{N}\bar{\boldsymbol{q}}\,\mathrm{d}\Gamma_1.$$

For Eq. (11) the approximation leads to the system

$$\mathbf{M}\dot{\mathbf{s}} + (\mathbf{D} + \mathbf{K} + \mathbf{C})\,\mathbf{s} = \mathbf{f}$$

Fig. 1 Evolution of the phase field in mode I tension. The model is a unit square $(x, y) \in [0, 1] \times [0, 1]$ with an initial crack length of 0.5 and loaded with a total prescribed displacement of $u = 1.2 \cdot 10^{-3}$ by means of a linear increasing loading factor

with $\mathbf{s} = [s_i]$ and

$$\mathbf{M} = \frac{1}{M} \int_\Omega \mathbf{N}\mathbf{N}^T \, d\Omega, \quad \mathbf{D} = \int_\Omega \left(\boldsymbol{\epsilon}^T \mathbb{C} \boldsymbol{\epsilon} \right) \mathbf{N}\mathbf{N}^T \, d\Omega, \quad \mathbf{K} = 2G_c l_c \int_\Omega \nabla\mathbf{N}\nabla\mathbf{N}^T \, d\Omega,$$

$$\mathbf{C} = \frac{G_c}{2l_c} \int_\Omega \mathbf{N}\mathbf{N}^T \, d\Omega, \quad \mathbf{f} = \frac{G_c}{2l_c} \int_\Omega \mathbf{N}\mathbf{N}^T \mathbf{1} \, d\Omega.$$

After the discretization in time by means of the implicit Euler scheme, the following system of equations is obtained:

$$\underbrace{\left[\frac{\mathbf{M}}{\Delta t} + \mathbf{D} + \mathbf{K} + \mathbf{C} \right]}_{\mathbf{A}} \mathbf{s}^{n+1} = \underbrace{\mathbf{f} + \frac{\mathbf{M}}{\Delta t} \mathbf{s}^n}_{\mathbf{b}}$$

2.2 Parameter of the fracture model

Whereas the critical fracture energy density—or critical energy release rate—G_c has a clear physical meaning, the parameter l_c and M are part of the specific phase-field approach to fracture. In order to illustrate their effect on the numerical solution, we consider a simple mode-I crack in a unit square as displayed in Fig. 1a. In this example, all values are given in a dimensionless way.

Clearly, the initial crack will grow straight till complete failure. During computation, the mobility constant M determines the velocity of the decrease in the phase-field parameter ₅. An increase in M leads to an accelerated crack evolution—more precisely in an equal number of timesteps ₅ will proceed to a lower value. In the quasi-static regime with $M \to \infty$, the local dissipation is prevented whereas low values of M facilitate high amounts of dissipation. Furthermore one can consider the mobility as the inverse of a viscosity η. Thus, a low value of M is equivalent to a pronounced viscous material behavior. Therefore, small mobility values are not permitted in our phase-field approach to linear elastic fracture.

In order to indicate a crack, the phase-field needs to change from 1 to 0. This requires parameter l_c to be significantly larger than the finite element mesh size h. Parametric studies recommend a value of $l_c \approx 6h$ to give smooth and mesh-independent results for piecewise linear shape functions of the finite elements [24]. The minimum size of $l_c \geq 3h$ corresponds to other studies, see [15,16]. If l_c is smaller, the phase-field solution tends to oscillate, and eventually, no crack will evolve.

For the example of the simple mode-I crack, the phase field ₅ around the crack is plotted for different values of l_c in Fig. 2. We clearly see the effect of l_c on the diffusity of the interface, i.e., on the crack width a—corresponding to the results presented in [25] and [20] where the influence of a small scale parameter is examined in an eigenfracture approach.

(a) l_c vs. half crack width a

(b) phase field $\mathfrak{s}(0.9, y)$
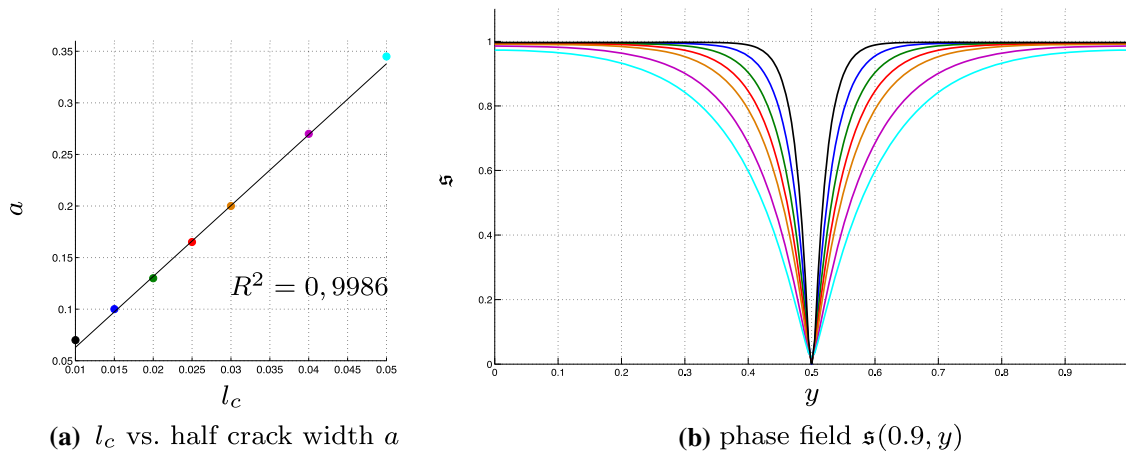
Fig. 2 Effect of the length parameter l_c on the width of the crack in the converged state of the mode-I crack model of Fig. 1. In **a** the half crack width a as a function of l_c for a linear regression with coefficient of determination $R^2 = 0,9986$ is displayed, and **b** diffuse interface marked by the phase field function $\mathfrak{s}$ perpendicular to the crack

(a)   **(b)**   **(c)**
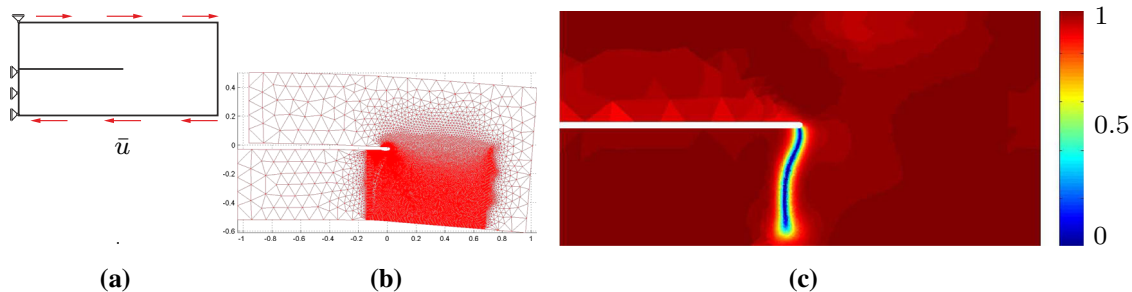
Fig. 3 Crack propagation in sliced block. The model of size $x, y \in [-1, 1] \times [0, 1]$ has an initial crack of length 1 and is sheared with a total prescribed displacement of $\bar{u} = \pm 2 \cdot 10^{-3}$ by means of a constant loading factor. **a** Model. **b** Deformed mesh. **c** Phase field

In Fig. 3, a sliced block is sheared in a way that the upper part is pulled to the right, whereas the lower part is moved in the opposite direction. In consequence, the original crack will propagate. Because the block is free of additional constraints, the initial mode-II fracture is not expected to remain shear-dominated. Instead, the crack kinks and grows in a mode-I dominated state. The example illustrates that the direction of crack propagation strongly depends on the model, specifically its boundary conditions. Additional influence has the finite element mesh in correspondence with parameter l_c. As we illustrated before, $l_c \geq 3h$ is recommended. If l_c is set small, only in an accordingly fine mesh the phase-field model can compute a crack. This implies that the crack will not be able to propagate into a coarse finite element mesh. In this sense, an predefined mesh refinement—as shown in Fig. 3—manipulates the direction of crack propagation.

3 Critical energy release rate of silicon dies

The integrated circuit unit of every microelectronic compound is commonly built on single-crystal silicon wafers that possess a high level of purity and perfection. The raw silicon to be used for this purpose is produced from silicon ingots which are sliced into thin wafers. As a consequence of fabrication, silicon dies show different populations of flaws which, in turn, cause a broad distribution of strengths and failure loads.

Failure experiments on such silicon dies are typically performed using simple geometries, e.g., three-point bending tests, where the applied load is increased progressively until fracture occurs. Statistical strength parameters are then determined from the experimental data. Here we refer to three-point bending experiments conducted at TU Berlin, see [2,21], with the setup illustrated in Fig. 4.

A set of 38 specimens has been tested. The die of thickness $l_t = 0.29$ mm was supported by two 2-mm-diameter beams with 4 mm distance, and the load has been applied through a third beam in the middle of
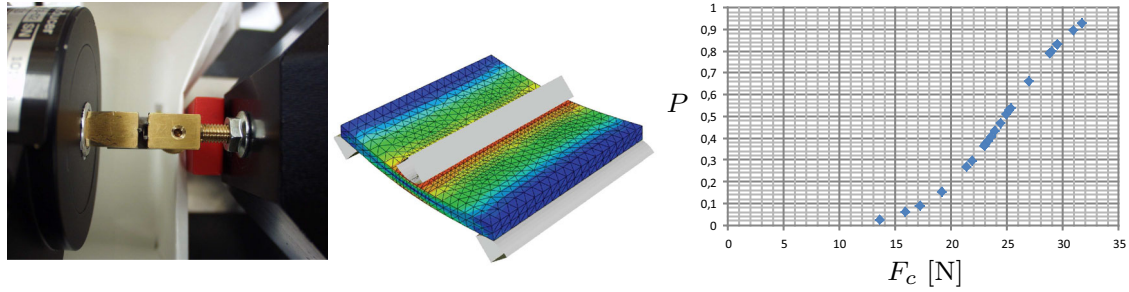
Fig. 4 Experimental setup of the three-point-bending experiments, 3d finite element simulation without fracture, cf. [22], and Weibull distribution of the failure load F_c

the 4.8×4.1 mm specimen. As a result, several specimens failed at very low loads, denoting a flawed (or otherwise weakened) population. Most of the specimens showed an intermediate strength with a failure load of $F = 24.2 \pm 4.6$ N.

Here, we want to use these results to determine the critical fracture energy density G_c of the dies. The (flawless) silicon material is characterized by an elastic modulus of $E = 163$ GPa. The die bends up to a maximum displacement of 0.023 mm which corresponds to a load of 25 N. This is about the failure load measured in the experiments. Similar results are obtained if we account for the anisotropy of single-crystal silicon in $\mathbb{C}$ with material parameters $C_{1111} = C_{2222} = C_{3333} = 165.8$ GPa, $C_{1122} = C_{1133} = C_{2233} = 63.9$ GPa and $C_{1212} = C_{1313} = C_{2323} = 79.6$ GPa. Please note that the strength values used in the calculation, and retrieved from the literature, are characterized by a large scatter, even as high as 70 % of the average value.

The die is a thin but stiff structure and in the dimensional reduction of a continuum to a quasi two-dimensional structure, the out-of-plane stress components are typically neglected. In this case, it is customary to assume a linearized model which is justified when the problem is characterized by small displacements and strains. It leads directly to the classical plate theories. In a Reissner–Mindlin plate model, the elastic strain tensor (2) is a function of the rotations of the plate normal $\boldsymbol{\vartheta} = (\vartheta_x, \vartheta_y)$, i.e., $\boldsymbol{\epsilon}(\boldsymbol{\vartheta}) = (\nabla \boldsymbol{\vartheta} + \nabla \boldsymbol{\vartheta}^T)/2$. Then, the weak form (10) is recast to:

$$\int_{\Omega} \boldsymbol{\epsilon}(\boldsymbol{\vartheta}) : \mathbb{C} : \boldsymbol{\epsilon}(\boldsymbol{\varphi}) \, l_t^3 \, \mathrm{d}\Omega + \int_{\Omega} \mu^* (\nabla w - \boldsymbol{\vartheta})^T (\nabla v - \boldsymbol{\varphi}) \, l_t \, \mathrm{d}\Omega = \int_{\Omega} \bar{p} w \, \mathrm{d}V \tag{12}$$

where

$$\mathbb{C} : \boldsymbol{\epsilon} = \frac{\lambda}{12} (\nabla \cdot \boldsymbol{\vartheta}) \mathbf{I} + \frac{\mu}{6} \boldsymbol{\epsilon}$$

with unit tensor $\mathbf{I}$; $\mu^* = {}^5\!/_6 \mu$ is a corrected shear modulus, and the load is $\bar{p} = F/(l_t A_{\text{load}})$. The weak form requires $(w, \boldsymbol{\vartheta}) \in H^1(\Omega) \times H^1(\Omega)^2$ and $(v, \boldsymbol{\varphi}) \in H_0^1(\Omega) \times H_0^1(\Omega)^2$, where H^1 denotes the Sobolev functional space of square integrable functions with square integrable weak derivatives and index 0 refers to homogenous boundary conditions. Equation (12) is solved together with the phase-field Eq. (11) in a staggered scheme.

Such a mixed problem generally requires a deeper mathematical analysis as an arbitrary choice of ansatz, and test spaces yield instabilities in the numerical solution. Here we employ a stable and locking-free finite element method outlined in [5,6] which allows an effective numerical treatment of the thin plate model. The results presented here refer to a uniform triangulation with $100 \times 100 \times 2$ elements, other (fine) meshes give very similar results. The critical length is set $l_c = 0.09$ mm.

We now assume a fracture energy density of $G_c = 0.01$ N/mm and apply a displacement of $w = 0.023$ mm within 10 loading steps by means of a linear increasing loading factor. After full loading in the middle of the specimen, a zone with $\mathfrak{s} = 0.5$ has shown, whereby the phase field reduces within 10 additional relaxation steps at fixed deflection. At next, we considered a slightly weakened specimen with a fracture energy density of $G_c = 0.007$ N/mm and we now observe a crack as displayed in Fig. 5. Within 10 steps of loading, the phase field reduces to zero in the loaded zone. Further reduction in G_c gives an early $\mathfrak{s} = 0$ zone, the structure is disintegrated, and further computation only refers to the artificial residual stiffness $\eta\mathbb{C}$. As a consequence, the $\mathfrak{s} = 0$ zone broadens in the course of computation. For example, a value of $G_c = 0.001$ N/mm shows a wide 'cracked' zone—indicating something like a totally damaged specimen. This does not correspond to brittle
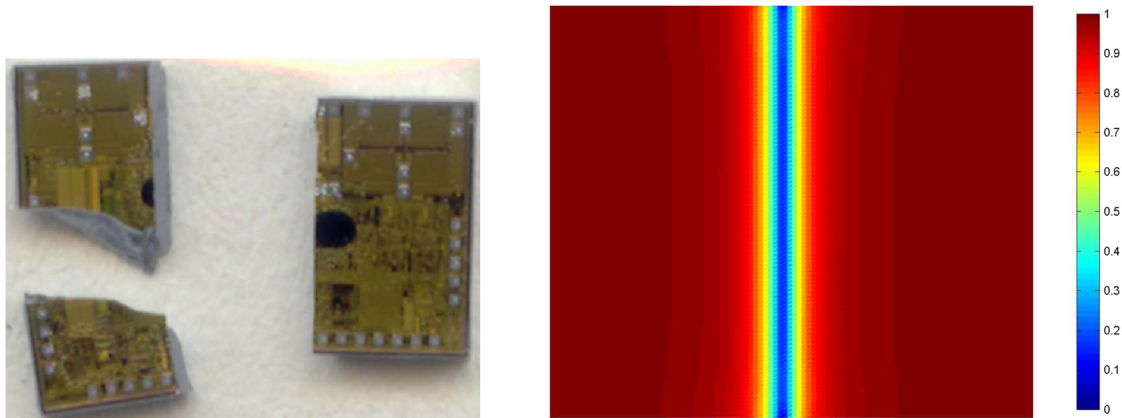
Fig. 5 Fracture of the silicon die; the displayed specimen failed at a final load of 22.1 N which is slightly below the average failure load. The phase field simulations shows the crack computed with $M = 25\,\text{mm}^2/\text{Ns}$, $l_c = 0.031$ mm and a critical energy release rate of $G_c = 0.007$ N/mm

fracture and, thus, with a too small value of G_c, the computed fracture pattern is not realistic. On the other hand, too large values of G_c do not lead to a significant lowering of the phase field within the 10 steps of loading. However, the phase field may reduce and a continued computation may lead to $\mathfrak{s} = 0$. This is a typical problem of static fracture simulations, its visibility depends on the choice of mobility M. The softening of the structure for $\mathfrak{s} < 1$, induced by a locally high elastic straining or even by numerical noise like boundary layer effects, leads the computation to converge to a crack ultimately. Therefore, it is necessary to keep a critical view on both, the final state of the quasi-static simulation and the evaluation of the $0 < \mathfrak{s} < 1$ values.

Alternatively, we directly apply a force $F = 25$ N on a zone of 0.3 mm width in 10 steps. With a fracture energy density of $G_c = 0.007$ N/mm, we again observe the crack in the middle of the specimen, but because of the wider loading area, the phase field is less localized here. Although the problem of crack definition remains the same, we found that a higher value of G_c stops crack growth. Additionally, a reduced load, e.g., $F = 10$ N does not induce any crack growth -independent of the value of G_c.

As a result, we may state that an inverse analysis of plate cracking with a phase-field approach to fracture is possible and leads to surprisingly exact predictions of the critical energy release rate G_c. Here, we determine a value of $G_c = 0.005$–0.007 N/mm which corresponds very well to the literature, cf. [21]. In all our computations, the crack grows along the loading axis but no cracks are observed for $G_c > 0.01$ N/mm. In order to see crack branching and fragmentation, however, we would have to leave the static regime of our simulation. Additionally, to account for variability of the strength, the deterministic approach used here should be abandoned and replaced by probabilistic methods, see [19].
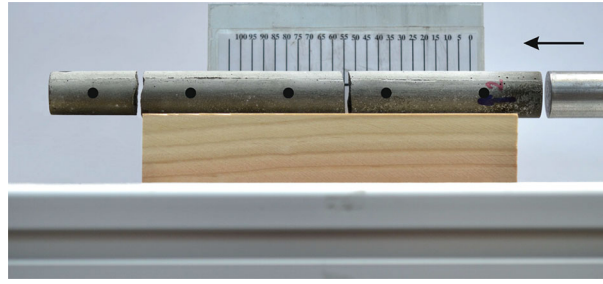
It remains to say that the brittle fracture in silicon dies is usually preceded by a certain amount of deformation, in some cases small but often falling in the range of moderate deflections. Consequently, plate models based on a linearized kinematic do not necessarily cover all possible experimental setups and may need to be replaced by moderate plate bending theories such as the models of von Karman or Wolmir [27].

## 4 Dynamic fracture of UHPC in a Hopkinson bar test

The experimental setup of a Hopkinson bar test consists of a cylindrical steel projectile which is accelerated by an air gun, a steel incident bar, and an apposed UHPC specimen. The impact of the striker generates a compressive stress pulse traveling through the incident bar and the specimen. At the free end of the specimen, the stress is reflected back as a tensile pulse. If the superposition of both pulses is beyond the dynamic tensile strength of the material, a fracture occurs, see Fig. 6. Such an experimental setup has been used in order to determine the fracture properties of an ultra-high-performance concrete (UHPC) material, see [13].

For the finite element analysis of the Hopkinson bar test, one can assume an axisymmetric state. The balance of momentum (1) with the specific Neumann boundary condition of the bar experiment reads:

$$\rho\ddot{\boldsymbol{u}} - \operatorname{div}\boldsymbol{\sigma} = 0 \quad \text{in } \Omega = [0, r_s] \times [0, l]$$
$$\boldsymbol{n}\boldsymbol{\sigma} = \bar{\boldsymbol{q}}(t) \quad \text{at } \Gamma_1 = \{(r, z) \in \Omega : z = l\} \subset \partial\Omega$$

Fig. 6 Hopkinson-Bar spallation experiment of UHPC, the incident bar is *left* of the specimen. Only the first crack in the *middle* of the specimen is considered in the simulations, the *right* crack happens later
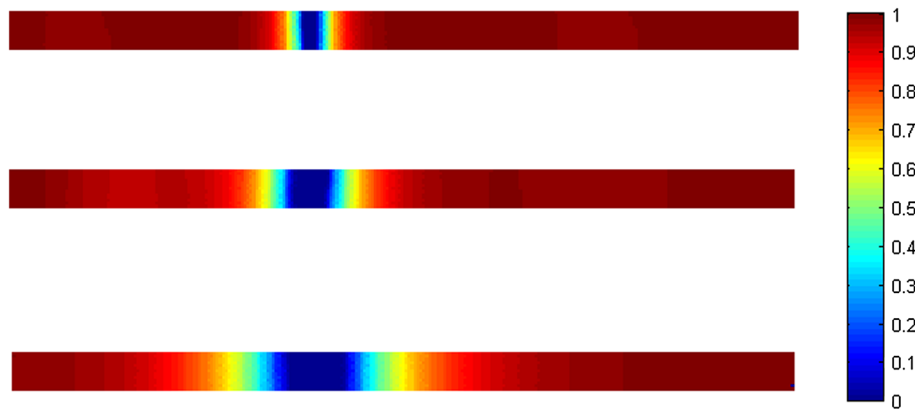
Fig. 7 Influence of l_c on the crack evolution: Phase-field parameter $\mathfrak{s}(\boldsymbol{x}, t = 120\,\mu s)$ for $l_c = 3h_{\min}, 6h_{\min}, 12h_{\min}, M = 30\,\mathrm{m}^2/\mathrm{(Ns)}, G_c = 90\,\mathrm{N/m}, \sigma_{\max} = 17.3\,\mathrm{MPa}$

Here r_s and l denote radius and length of the specimen. The incoming stress pulse $\mathbf{q}(t)$ is modeled with a trapezoidal approximation where $\sigma_{\max} = \max\{\bar{\mathbf{q}}(t)\}$ denotes the maximum stress. We use material parameters of UHPC, $E = 59\,\mathrm{GPa}, \nu = 0.2, \rho = 2370\,\mathrm{kg/m}^3$ and realistic (measured) values for the specific fracture energy G_c of UHPC which are in the range of 75–200 N/m.

The mobility parameter M in Eq. (11) needs to be chosen in such a way that the phase-field is able to decrease locally to zero within a time range of few microseconds, once the energy release rate exceeds the specific fracture energy. Here we set $M = 30\,\mathrm{m}^2/\mathrm{Ns}$. Significant lower values of M lead to a retarded decrease of $\mathfrak{s}$ which is in contradiction to the results of the performed experiments.

Figure 7 illustrates the influence of length l_c on the width of the transition zone between intact and broken material as well as on the width of the damaged zone (the area with $\mathfrak{s} = 0$). As mentioned before, the minimum size of l_c depends on the finite element mesh size. Therefore, a fine mesh leads to improved results regarding the transition zone and the width of the crack. Simulations with fine meshes emphasize the influence of the choice of l_c on the fact whether a crack emerges during the simulation or not: For example, the evolution of a crack has been established for the parameters $G_c = 90\,\mathrm{N/m}, M = 10\mathrm{m}^2/\mathrm{(Ns)}, \sigma_{\max} = 17.3\,\mathrm{MPa}, h_{\min} \approx 6.3 \cdot 10^{-4}\,\mathrm{m}$ and $l_c = 4h_{\min}$, whereas for $l_c = 3h_{\min}$ the phase-field parameter just decreased to a minimum of ≈ 0.92. A very low value of l_c enables the suppression of the crack evolution due to the term $(1-\mathfrak{s})/2l_c$ in the evolution Eq. (8) which counteracts the energy density function term $\partial \Psi^e/\partial \mathfrak{s}$.

The specific fracture energy density G_c has a crucial effect on the crack evolution, see Fig. 8. If G_c is set to a high value, Griffith's criterion possibly cannot be fulfilled anymore, and the phase-field parameter $\mathfrak{s}$ remains at the constant value 1 during the whole simulation. Furthermore G_c influences the crack position and also the width of the damaged zone: A reduction in G_c leads to a movement of the crack position closer to the free end of the specimen. This is based on the fact that $\partial \Psi^e/\partial \mathfrak{s}$ exceeds the term on the right side in the evolution equation at an earlier point of time. Moreover, an increase in the width of the damaged zone is observed.

Another parameter that has an essential effect on the crack development is the maximum stress $\sigma_{\max}$ of the incoming stress pulse (see Fig. 9): A low value of $\sigma_{\max}$ leads to small strains and thus to slight values for Ψ^e -
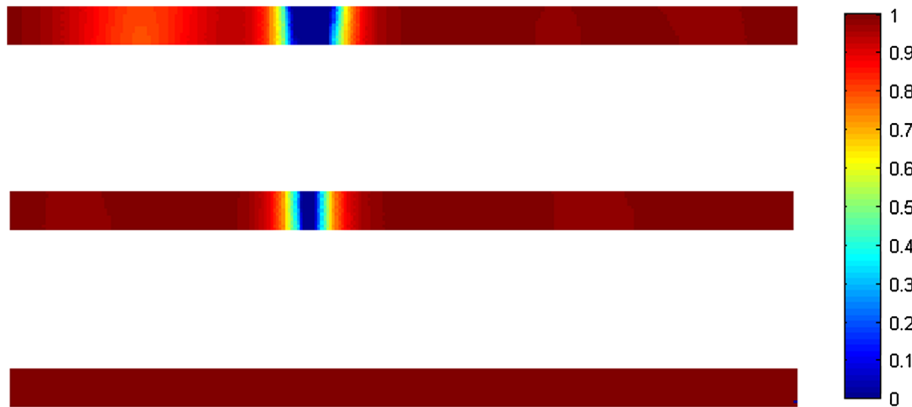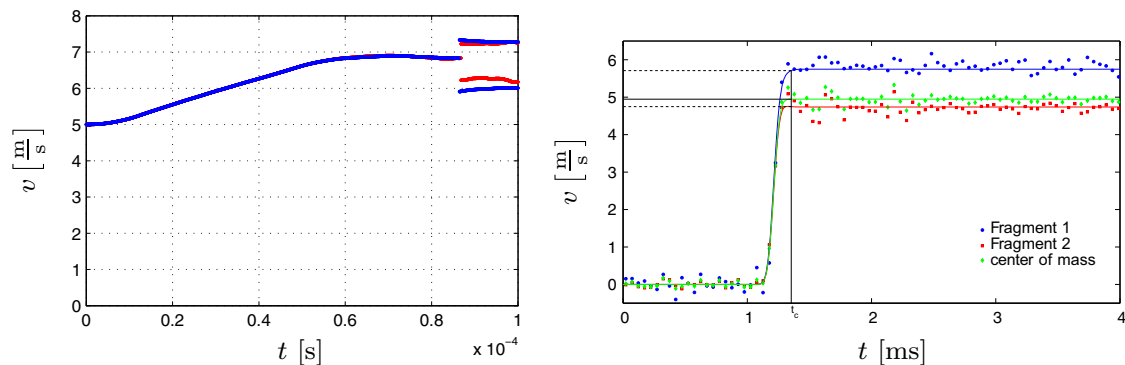
Fig. 8 Influence of critical energy release rate G_c on the crack evolution: phase-field parameter $\mathfrak{s}(x, t = 120\mu s)$ for $G_c = 40\,\text{N/m}, 90\,\text{N/m}, 360\,\text{N/m}, l_c = 3h_{\min}, M = 30\,\text{m}^2/(\text{Ns}), \sigma_{\max} = 17.3\,\text{MPa}$
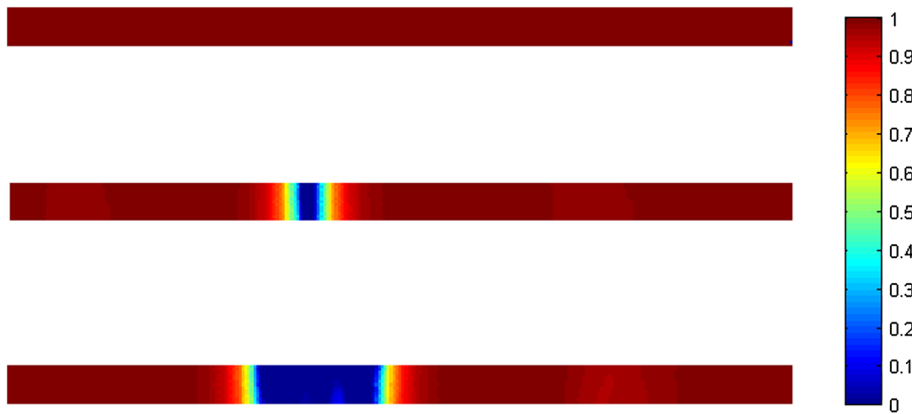
Fig. 9 Influence of initial stress maximum $\sigma_{\max}$ on the crack evolution: Phase-field parameter $\mathfrak{s}(x, t = 120\,\mu s)$ for $\sigma_{\max} = 10\,\text{MPa}, 17\,\text{MPa}, 50\,\text{MPa}, G_c = 90\,\text{N/m}, l_c = 3h_{\min}, M = 30\,\text{m}^2/(\text{Ns})$

Fig. 10 Computed velocity of the specimen before crack initiation (blue) and the 2 fragments after crack initiation assuming $G_c = 90\,\text{N/m}, l_c = 3h_{\min}, M = 30\,\text{m}^2/(\text{Ns}), \sigma_{\max} = 17.3\,\text{MPa}$. The result is compared to the velocities calculated by means of a cohesive element approach (*red*). For comparison on the right the experimental velocity-time diagram of the spallation experiment. The *red dots* represent the velocity of fragment 1 (average of 31 control points), the *blue squares* represent the velocity of fragment 2 (average of 8 control points) and the *green diamonds* represent the extrapolated initial center of mass velocity (color figure online)

the decrease of $\mathfrak{s}$ and the crack evolution is suppressed. However, an increase of $\sigma_{\max}$ supplies results similar to those based on low specific fracture energies: The crack position is located closer to the free end, and the width of the damaged zone increases.

Figure 10 illustrates the velocity of the specimen and of the two fragments after failure. We assume an initial velocity of $v_0 = 5$ m/sec for the specimen due to the acceleration of the incident bar and specific fracture energy of $G_c = 90$ N/m. Here a permanent crack is defined if the phase-field parameter $\mathfrak{s}$ is below a value of 0.3 over the whole width of the specimen. These calculated velocities are compared to the velocities computed with a cohesive element approach assuming the same energy density G_c and a linearly decreasing cohesive law. It becomes obvious that both approaches provide similar results especially before the crack initiation but also after fragmentation. Another observation is that the phase-field approach also provides according results concerning the difference of the fragments velocity measured in the experiments which is approximately 1 m/sec immediately after crack occurrence.

References

1. Bourdin, B., Francfort, G.A., Marigo, J.J.: The variational approach to fracture. J. Elast. **9**, 5–148 (2008)
2. Bohm, C., Hauck, T., Juritza, A., Müller, W.H.: Weibull statistics of silicon die fracture. In: Proceedings of ETPC (2004)
3. Borden, M.J., Hughes, T.J.R., Landis, C.M., Verhoosel, C.V.: A higher-order phase-field model for brittle fracture: formulation and analysis within the isogeometric analysis framework. Comput. Method Appl. Mech. Eng. **273**, 100–118 (2014)
4. Borden, M.J., Verhoosel, C.V., Scott, M.A., Hughes, T.J.R., Landis, C.M.: A phase-field description of dynamic brittle fracture. Comput. Method Appl. Mech. Eng. **217–220**, 77–95 (2012)
5. Carstensen, C., Weinberg, K.: Calculating the energy-norm fem-error for Reissner–Mindlin plates without known reference solution. Comput. Mech. **26**(6), 566–570 (2000)
6. Carstensen, C., Weinberg, K.: Adaptive mixed finite element method for Reissner–Mindlin plates. Comput Method Appl. Mech. Eng. **190**(51-52), 6895–6908 (2001)
7. Francfort, G.A., Marigo, J.-J.: Revisiting brittle fracture as an energy minimization problem. J. Mech. Phys. Solids **46**, 1319–1342 (1998)
8. Griffith, A.A.: The phenomena of rupture and flow in solids. Philos. Trans. R. Soc. Lond. **221**, 163–198 (1921)
9. Henry, H., Levine, H.: Dynamic instabilities of fracture under biaxial strain using a phase field model. Phys. Rev. Lett. **93**, 105505 (2004)
10. Hofacker, M., Miehe, C.: A phase field model of dynamic fracture: Robust field updates for the analysis of complex crack patterns. Int. J. Numer. Meth. Eng. **93**, 276–301 (2013)
11. Hesch C., Weinberg K.: Thermodynamically consistent algorithms for a finite-deformation phase-field approach to fracture. Int. J. Numer. Meth. Eng. (2014)
12. Irwin G.R.: Elasticity and plasticity: fracture. In: S. Függe, editor. Encycl. Phys. (1958)
13. Khosravani, M.R., Dally, T., Bogunia, L., Frohlich, D., Wagner, P., Trettin, J., Weinberg, K.: Dynamic fracture investigations of ultra-high performance concrete. Int. J. Solids Struct. (2014) (submitted for publication in)
14. Karma, A., Kessler, D.A., Levine, H.: Phase-field model of mode III dynamic fracture. Phys. Rev. Lett. **81**, 045501 (2001)
15. Kuhn, C., Müller, R.: A continuum phase field model for fracture. Eng. Fract. Mech. **77**, 3625–3634 (2010)
16. Miehe, C., Hofacker, M., Welschinger, F.: A phase field model for rate-independent crack propagation: Robust algorithmic implementation based on operator splits. Comput. Methods Appl. Mech. Eng. **199**, 2765–2778 (2010)
17. Miehe, C., Schänzel, L.M.: Phase field modeling of fracture in rubbery polymers. Part I: finite elasticity coupled with brittle failure. J. Mech. Phys. Solids **65**, 93–113 (2014)
18. Moes, N., Stolz, C., Bernard, P.-E., Chevaugeon, N.: A level set based model for damage growth: the thick level set approach. Int. J. Numer. Methods Eng. **86**(3), 358–380 (2001)
19. Phillips, R.: Crystals, Defects and Microstructures: Modeling Across Scales. Cambridge University Press, Cambridge (2001)
20. Pandolfi, A., Ortiz, M.: An eigenerosion approach to brittle fracture. Int. J. Numer. Meth. Eng. **92**, 694–714 (2012)
21. Pandolfi, A., Weinberg, K.: A numerical approach to the analysis of failure modes in anisotropic plates. Eng. Fract. Mech. **78**, 2052–2069 (2011)
22. Quade, H., Pandolfi, A., Weinberg, K.: Quasi-static failure modes of silicon dies. In: Proceedings of 12th International Conference on Fracture, Ottawa, ON, Canada (2009)
23. Spatschek, R., Brener, E.A., Karma, A.: Phase field modeling of crack propagation. Philos. Mag. **91**, 75–95 (2010)
24. Scheid, M.: FEM-Berechnung der Rissausbreitung mittels Phasenfeldmethode. BSc Thesis, Siegen University (2014)
25. Schmidt, B., Fraternali, F., Ortiz, M.: Eigenfracture: an eigendeformation approach to variational fracture. Multiscale Model. Simul. **7**, 1237–1266 (2009)
26. Verhoosel, C.V., de Borst, R.: A phase-field model for cohesive fracture. Int. J. Numer. Methods Eng. **96**, 43–62 (2013)
27. Wolmir, A.S.: Biegsame Platten und Schalen. Springer, Berlin (1962)